Downloaded from orbit.dtu.dk on: May 14, 2024

DTU Library

Computational fluid dynamic modeling of liquid-gas flow patterns and hydraulics in the cross-corrugated channel of a plate heat exchanger

Zhu, Xiaowei; Haglind, Fredrik

Published in:
International Journal of Multiphase Flow

Link to article, DOI:
10.1016/j.ijmultiphaseflow.2019.103163

Publication date:
2020

Document Version
Publisher's PDF, also known as Version of record

Link back to DTU Orbit

Citation (APA):
Zhu, X., & Haglind, F. (2020). Computational fluid dynamic modeling of liquid-gas flow patterns and hydraulics in the cross-corrugated channel of a plate heat exchanger. *International Journal of Multiphase Flow*, *122*, Article 103163. https://doi.org/10.1016/j.ijmultiphaseflow.2019.103163

General rights
Copyright and moral rights for the publications made accessible in the public portal are retained by the authors and/or other copyright owners and it is a condition of accessing publications that users recognise and abide by the legal requirements associated with these rights.

- Users may download and print one copy of any publication from the public portal for the purpose of private study or research.
- You may not further distribute the material or use it for any profit-making activity or commercial gain
- You may freely distribute the URL identifying the publication in the public portal

If you believe that this document breaches copyright please contact us providing details, and we will remove access to the work immediately and investigate your claim.

International Journal of Multiphase Flow 122 (2020) 103163

Contents lists available at ScienceDirect

International Journal of Multiphase Flow

journal homepage: www.elsevier.com/locate/ijmulflow

Computational fluid dynamics modeling of liquid–gas flow patterns and hydraulics in the cross-corrugated channel of a plate heat exchanger

Xiaowei Zhu*, Fredrik Haglind

Department of Mechanical Engineering, Technical University of Denmark, Nils Koppels Allé, Building 403, 2800 Kongens Lyngby, Denmark

ARTICLE INFO

Article history:
Received 12 July 2019
Revised 7 November 2019
Accepted 11 November 2019
Available online 12 November 2019

Keywords:
Plate heat exchanger
Cross-corrugated channel
Two-phase
Computational fluid dynamics
Flow pattern

ABSTRACT

The morphology of liquid–gas flows in corrugated plate heat exchangers is complex due to the intricate channel geometry. To date, only a few experimental visualizations have been performed to study the two-phase flow characteristics in plate heat exchangers. In this paper, we perform pioneering computational fluid dynamics simulations of the adiabatic liquid–gas (water-air) flow in a cross-corrugated channel of a plate heat exchanger. The standard volume-of-fluid technique is used to capture the complex phase-interfaces constructed by the cross-corrugated walls. In order to reduce the computational cost, the computational domain is simplified by a series of assumptions. The bubbly flow, slug flow, churn flow and film flow are modeled by varying the superficial velocities of both phases, and the validity of these patterns is proved by comparison with experimental results. A flow regime map is developed based on the numerical results, and the transitions between the regimes are discussed. The predicted pressure drop shows good agreement with the experimental data. The two-phase multiplier for general prediction of the friction factor in the cross-corrugated channel is calibrated. The mean void fraction in the channel is quantified by the numerical simulation. The void fraction model from Zuber and Findlay is found to be applicable to the cross-corrugated channel, which is further modified for general use for these types of channel flows.

© 2019 Elsevier Ltd. All rights reserved.

1. Introduction

The chevron plate heat exchanger (PHE) is one of the most efficient and compact of the heat transfer equipment in the commercial market. The PHE consists of multilayers of corrugated plates stacked together in a criss-cross manner, forming the so-called cross-corrugated channels; see Fig. 1. The hot and cold fluids flow alternatively in the neighboring channels, effectively exchanging heat. In modern industries, the PHE is often used as an evaporator or condenser for cooling, heating, and power generation applications.

Extensive experimental research about the flow evaporation/condensation in PHEs have been reported in open literature and were comprehensively reviewed by (Amalfi et al., 2016). However, most of those works only focused on the measurement of global thermal-hydraulic performances, and poorly investigated the basic flow characteristics in PHEs. A few experimental visualizations in cross-corrugated channels have been performed; these works are summarized in Table 1. These literature studies show the evidence of diverse flow patterns possibly occurring in the PHE, including bubbly flow, slug flow, churn flow and film flow. The observed flow pattern seems strongly dependent on the channel geometric parameters, working fluids, as well as the operating conditions. In a recent literature review Tao et al. (2017) plotted a flow regime map for the PHE based on results of previous works. It is hard either to find consistencies among the works or distinguish the boundaries between different flow regimes from the map, probably due to the differences in experimental setups, as well as the subjectivity of observers when judging the flow pattern. Tao et al. (2017) comments that the existing database of the two-phase flow patterns in PHEs is associated with high uncertainty. More investigations in this direction are strongly needed in order to find consistent knowledge about the two-phase flow characteristics, which is crucial for the design of PHE products.

Nowadays, the two-phase flows can be simulated numerically by using computational fluid dynamics (CFD) methods (Kharangate and Mudawar, 2017). The CFD methods provide many advantages over the state-of-the-art experimental approaches, especially for quantitative analysis of the flow physics. For instance,

* Corresponding author.
E-mail address: xiaozhu@mek.dtu.dk (X. Zhu).

https://doi.org/10.1016/j.ijmultiphaseflow.2019.103163
0301-9322/© 2019 Elsevier Ltd. All rights reserved.

Nomenclature

b	amplitude of the corrugation, mm
D_h	hydraulic diameter, $D_h = 4b/\varphi$, mm
f	friction factor
F_{CSS}	surface tension force, N
g	gravity acceleration, m/s^2
G	mass flux, kg /m^{2}s
I	unit tensor
L	length of the domain/channel, mm
P	pressure, Pa
Re	Reynolds number, $Re = GD_h/\mu$
t	time, s
u	velocity, m/s
V	control volume, m^3
W	width of the domain/channel, mm
x	gas quality
X	Lockhart–Martinelli parameter

Greek symbols

α	void fraction
β	corrugation angle
θ_w	contact angle
μ	viscosity, Pa s
ρ	fluid density, kg m^{-3}
σ	surface tension, N m^{-1}
φ	enlargement factor of the plate
ϕ_L	two-phase multiplier
Δ	gradient of variables
Λ	pitch of the corrugation, mm

Subscripts

dr	drift
eff	effective
g	Gas
l	liquid
linear	linear range
m	mixture

the void fraction of a multiphase system is tricky to be measured experimentally, while it can be easily calculated via the CFD approach. However, the multiphase CFD simulation is usually computationally expensive and relies on the use of high resolution grids if the interface tracking is required, which limits the widespread application of CFD in modeling the complex two-phase flows often encountered in engineering practices, such like the two-phase flow in PHEs. To the best of the authors' knowledge, no CFD simulation on the two-phase flow in PHEs has been reported in open literature. The major challenge lies in the construction of high quality grids for the cross-corrugated channel. In addition, the associated computational costs to model the entire flow path of the PHE are tremendous.

Nevertheless, some relevant CFD activities for structured packing columns are worth mentioning here because the structured packing is also featured with cross-corrugated passages, which resemble the flow passages of the PHE. In recent years, CFD modeling is frequently used to explore the interfacial phenomena in the structured packing, such as liquid hold-up distribution and interfacial area (Sacher and Repke, 2019; Singh et al., 2018; Sun et al., 2013). Despite the resemblance of the channel geometry, the working principles of the structured packing and the PHE are very different in terms of the flow arrangement. The liquid and gas are usually countercurrent in the structure packing, while they are in co-current flow in the PHE. Therefore, the PHE requires a different CFD approach to predict the co-current two-phase flow behaviors.

This paper presents, for the first time, a CFD-based study of co-current liquid–gas flows in the cross-corrugated geometry of a plate heat exchanger, under adiabatic conditions. The study aims to gain a better understanding of the two-phase flow patterns in the PHE and to develop correlations to quantify the pressure drop and void fraction in the PHE based on the CFD results. In order to resolve well the phase interface, the standard volume-of-fluid (VOF) technique is used, and high quality hexahedral grids are deployed for the computational domain. The simulated flow patterns including bubbly flow, slug flow, churn flow and film flow are disclosed and interpreted, and a flow regime map based on the numerical results is proposed and discussed. The two-phase multiplier is calibrated for a better prediction of the friction factor in the PHE. Furthermore, the void fraction in the PHE is quantified based on results from the CFD simulations, and a rational model to estimate the mean void fraction in a cross-corrugated channel is derived.

The paper is organized as follows. In Section 2, the mathematical models, assumptions and computational details are given. In Section 3, the pressure drops of both single- and two-phase flows in the cross-corrugated channel are presented and validated against experimental data. The simulated flow patterns are presented and discussed in Section 4; in Section 5, the flow regime map is presented; in Section 6, the mean void fraction is quantified and correlated with gas quality and mass flux; the conclusions and final remarks are summarized in Section 7.

2. Computational approach

2.1. Governing equations

In the present study, the immiscible liquid–gas flow in the cross-corrugated channel was solved by using the ANSYS Fluent 18.2, a finite-volume based solver. The standard volume-of-fluid (VOF) technique was adopted to track the interface. The mass

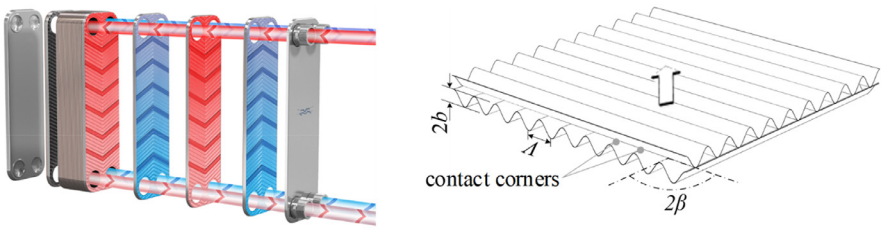

(a) (b)

Fig. 1. (a) The typical configuration and assembly of a commercial plate heat exchanger, which consists of numbers of corrugated plates (by courtesy of Alfa Laval). Hot stream (red) and cold stream (blue) flow alternatively in neighboring channels. (b) A detail schematic of the cross-corrugated channel, where $\boldsymbol{b}$, $\boldsymbol{\Lambda}$ and $\boldsymbol{\beta}$ are corrugation amplitude, corrugation pitch and inclination angle, respectively. (For interpretation of the references to color in this figure legend, the reader is referred to the web version of this article.)

Table 1
Summary of previous works on experimental visualization of liquid–gas flows in cross-corrugated channels.

References	Geometric dimensions	Fluids (liquid–gas)	Flow direction	Operation condition	Observed flow patterns
Xu and Carey (1987)	$\Lambda = 8.55b = 1.2\beta = 30^\circ$	Water	Upward & horizontal	Boiling	For upward case: churn flow and annular flow; for horizontal case: wavy flow and annular flow.
Gradeck and Lebouché (2000)	$\Lambda = 65b = 10\beta = 65^\circ, 90^\circ$	Water-nitrogen	horizontal	Adiabatic	Bubbly flow and stratified flow.
Tribbe and Müller-Steinhagen (2001a)	$\Lambda = 12b = 1.5,\ 1\beta = 30^\circ, 60^\circ$	Water-air	downward	Adiabatic	Bubbly flow, irregular bubbly flow, churn flow, film flow, and partial film flow.
Vlasogiannis et al. (2002)	$\Lambda = 10b = 1.2\beta = 60^\circ$	Water-air	downward	Adiabatic	Continuous gaseous flow, bubbly flow, and slug flow.
Hsieh et al. (2002)	$\Lambda = 10b = 1.65\beta = 60^\circ$	R-134a	upward	Subcooled boiling	Bubbly flow.
Nilpueng and Wongwises (2010)	$b = 1.25\beta = 57.5^\circ$	Water-air	Downwardupward	Adiabatic	For upward case: Bubbly flow and annular-liquid bridge flow; for downward case: bubbly flow, slug flow, and annular-liquid bridge flow.
Solotych et al. (2016)	$\Lambda = 5.7,\ 3.7b = 1.0, 0.5\beta = 60^\circ, 65^\circ$	HFE-7100	upward	Adiabatic	Bubbly flow, churn flow, and film flow
Grabenstein et al. (2017)	$\Lambda = 11.4b = 1.5\beta = 27^\circ, 63^\circ$	R365mfc water-air	downward	Adiabaticand boiling	Bubbly flow, slug flow, churn flow, and film flow
Jin and Hrnjak (2017)	$\Lambda = 10b = 1.1\beta = 60^\circ$	R245fa	Upwarddownward	Adiabaticand boiling	For upward case: liquid pool, irregular bubbly flow, film flow and liquid dry-out; for downward case: film flow and dry-out
Kim et al. (2019)	$\Lambda = 7b = 1\beta = 60^\circ$	R-245fa	Upward	Adiabatic	Bubbly flow and partial film flow
(Lee et al., 2019)	$\beta = 60^\circ$	R-1234ze(E)	Upward	Adiabatic	Five dominant flow regimes were observed: slug flow, wavy liquid film flow, pulsating annular flow, vapor-preferred path annular flow, and entire annular flow.

conservation equations were solved for liquid and gas phases, separately.

For the liquid phase:

$$\frac{\partial}{\partial t}(\alpha_l \rho_l) + \nabla \cdot (\alpha_l \rho_l \vec{u}) = 0 \tag{1}$$

For the gas phase:

$$\frac{\partial}{\partial t}(\alpha_g \rho_g) + \nabla \cdot (\alpha_g \rho_g \vec{u}) = 0 \tag{2}$$

Since only two phases are presented, $\alpha_l + \alpha_g = 1$.

The forces of pressure, friction, gravity and surface tension, acting on the fluid flow, are included in a single set of momentum equations shared for both phases, expressed as

$$\frac{\partial}{\partial t}(\rho_m \vec{u}) + \nabla \cdot (\rho_m \vec{u}\vec{u}) = -\nabla P + \nabla \cdot \left[\mu_{eff}\left(\nabla \vec{u} + \nabla \vec{u}^T\right)\right] + \rho \vec{g} + \vec{F}_{css} \tag{3}$$

where $\rho_m = \rho_l \alpha_l + \rho_g \alpha_g$, and $\mu_{eff} = \mu_l \alpha_l + \mu_g \alpha_g + \mu_t$.

The surface tension force $\vec{F}_{css}$ in the momentum equation was modeled based on the continuum surface stress concept (ANSYS, 2018), written as

$$\vec{F}_{css} = \nabla \cdot \left[\sigma |\nabla \alpha| I - \frac{\nabla \alpha \otimes \nabla \alpha}{|\nabla \alpha|}\right] \tag{4}$$

The k -ω shear-stress-transport (SST) model (Menter, 1994) was applied to close the Reynolds stress term. However, the k-ω model generally overpredicts the turbulence intensity near the liquid–gas interface because of the high velocity gradient in the interfacial area (Kharangate and Mudawar, 2017). This defect can be mitigated by adding a turbulent damping source term to the ω-equation according to (Egorov, 2004). The study of Kharangate et al. (2015) showed that the k-ω SST model, incorporated with the Egorov's turbulent damping model, can yield a nice prediction of the interfacial quantities of falling films. Accordingly, the turbulent damping formula of Egorov with a damping factor of 10 was used in the present simulations to improve the turbulent prediction in the liquid–gas interfacial area.

2.2. Computational domain and grid construction

For validation purposes, the geometry of the cross-corrugated channel used for simulations is identical to Tribbe and Müller-Steinhagen's experimental prototype (Tribbe and Müller-Steinhagen, 2001a,b). The key geometric parameters are listed in Table 2 (also see Figs. 1 and 2 for the definition of each parameter). In order to model an entire flow channel of the considered PHE, the required grid size was preliminarily estimated to need at least 66 million nodes. The associated computational cost would be unaffordable. To save the cost, the size of the computational domain was reduced based on the following assumptions. Firstly, the flow was assumed to be uniformly spanned in the channel without maldistribution; secondly, the flow pattern was assumed to be periodic in the spanwise direction of the channel. Thirdly, it was assumed that the flow characteristics are not influenced by the streamwise length of the domain once the flow is fully developed. Given these preconditions, the domain size was reduced to 1/50 of the entire channel dimension, as shown in Fig. 2, and so were the computational costs. The streamwise length of the domain was determined to be 1/3 of the total channel length, which is long enough to enable the flow pattern to be fully developed along the streamwise direction.

The hexahedral grids were deployed to the entire computational domain as shown in Fig. 2. The contact corners are the places where the two opposite corrugation plates are attached, which were represented by hollow spots. The grid consists of 1.33

Table 2
Geometric dimensions of the computational domain and the PHE in the reference literature.

References	L, mm	W, mm	β	b, mm	Λ, mm	φ
Computational domain	127	22	60	1.5	11	1.166
Tribbe and Müller-Steinhagen (2001a)	640	240	60	1.5	11	1.166
Jin and Hrnjak (2017)	495	210	60	1.1	10	1.111
Focke et al. (1985)	400	100	60	2.5	10	1.473

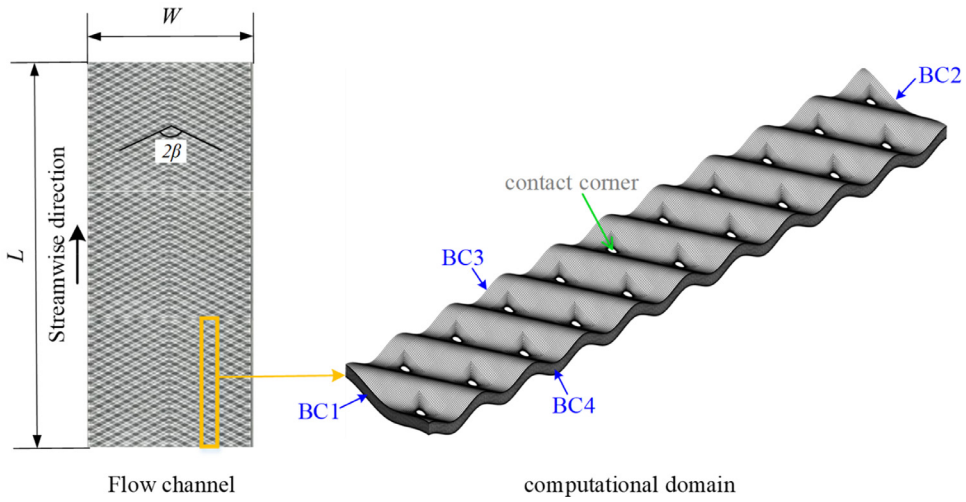

Fig. 2. Simplification of computational domain from a whole cross-corrugated channel, and the grid details.

million nodes in total. A preliminary grid sensitive test was performed, which suggests that a grid size of 0.89 million is sufficient to predict the two-phase flow pressure drop reasonably, while the resolution of captured interface is compromised. Therefore, the finer grid was used to ensure the flow pattern was captured with high resolution. In particular, the near wall grid was carefully refined to ensure the y^+ close to or smaller than unity for all simulations. The distance of the first layer nodes normal to the wall is around 5–10 μm, so that the near wall liquid film can be well treated.

2.3. Working fluids

Consistent with the experimental condition of Tribbe and Müller-Steinhagen (2001b), the water-air combination was used as the working fluid. The fluid properties were evaluated under the conditions of 25 °C (temperature) and 2 bar (pressure). For water, $\rho = 997.1\,\mathrm{kg/m^3}$, and $\mu = 8.9 \times 10^{-4}$ Pa s; for air, $\rho = 2.36\,\mathrm{kg/m^3}$, and $\mu = 1.85 \times 10^{-5}$ Pa s. The fluid properties were assumed to remain constant during the simulation. The surface tension between water and air is 0.072 N/m . It was assumed that the water-air system has a fixed contact angle θ_w with the wall, which is 81°.

2.4. Boundary conditions

Referring to Fig. 2, the notation BC1 represents the mass flow inlet; the mass flux of liquid and gas are explicitly specified as $G_g = x\ G$ and $G_l = (1-x)G$, respectively. The notation BC2 corresponds to the pressure outlet, where a constant static pressure of 0 Pa is assigned. The notations BC3 and BC4 are defined as the transversal periodical boundary condition. A zero pressure-gradient is imposed in the transversal direction. Given this periodical assumption, all the flow quantities on the BC3 and BC4 surfaces are identical. At the walls, the no-slip condition is assigned. A dynamic boundary condition is applied to the wall's adjacent cells to account for the wall adhesion effect. With the contact angle θ_w being known, the interface curvature is adjusted in the simulation using the equation $\hat{n} = \hat{n}_w cos\theta_w + \hat{\tau}_w sin\theta_w$ (Brackbill et al., 1992), where $\hat{n}$ is the interface normal at the live cells near the wall; $\hat{n}_w$ and $\hat{\tau}_w$ are the unit vectors normal and tangential to the wall, respectively. The local curvature of the interface is determined using the contact angle and the calculated surface normal one cell away from the wall.

2.5. Solution techniques

Eqs. (1) and (2) are discretized using the implicit formulation, with the default value of 1×10^{-6} for the volume fraction cutoff. The PISO scheme is used to tackle the pressure–velocity coupling. The PRESTO! scheme is used for pressure discretization. The moment and turbulent equations are discretized based on a second-order upwind scheme. The phase interface is constructed by applying a modified High Resolution Interface Capturing (HRIC) technique. The temporal discretization is based on the bounded second-order implicit formulation. Before the computation, the flow field is initialized with zero velocity and zero void fraction. For two-phase modeling, the simulation is run with adaptive time steps to ensure the global Courant Number is smaller than unity for every time step. The simulations were performed on the Niflheim supercomputer at DTU Campus Lyngby.

3. Pressure drop

3.1. Single-phase pressure drop

Prior to the two-phase simulation, the single-phase flow in the cross-corrugated channel is modeled. The single-phase results serve as a preliminary reference to validate partially the numerical model. Fig. 3(a) shows the pressure fluctuation monitored at the channel inlet for Re=145. The results indicate that flow chaotically oscillates even at such a low Reynolds number. Therefore, it is necessary to take time-averaging of the pressure field in order to obtain the mean pressure drop along the channel. The sampled time interval for making the average is highlighted in Fig. 3(a), and

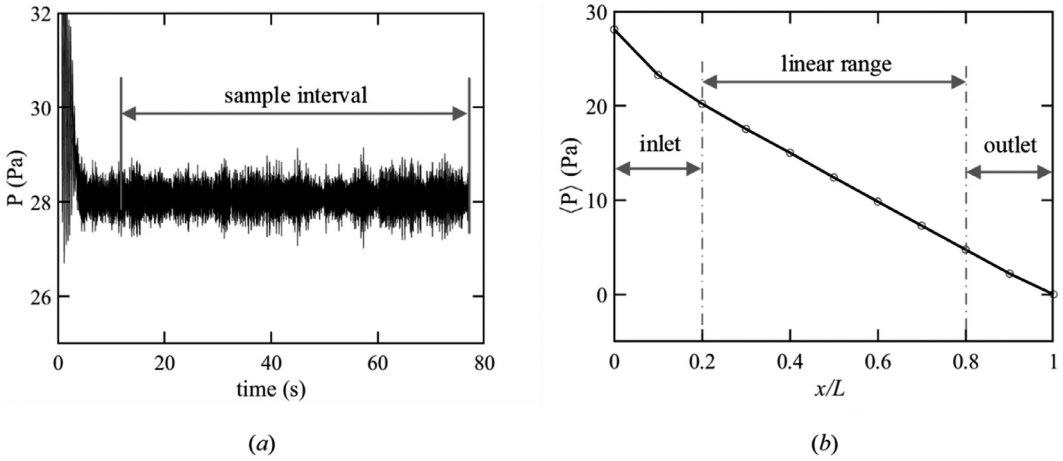

Fig. 3. The way to evaluate the mean pressure drop along the channel. (a) Time history of static pressure monitored at the inlet ($x = 0$) of the channel at $Re = 145$. The sample interval for taking the time-averaging calculation is marked. (b) Time averaged pressure along the streamwise direction. The mean pressure drop per unit length is evaluated within the linear range.

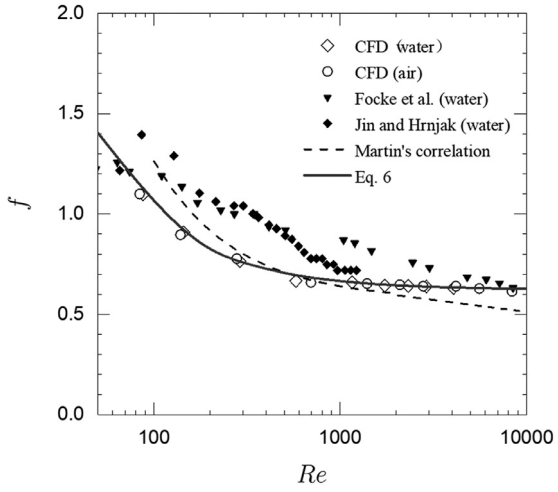

Fig. 4. Comparisons of the friction factor of single-phase flow predicted by CFD, correlations and the experimental results fromprevious works.

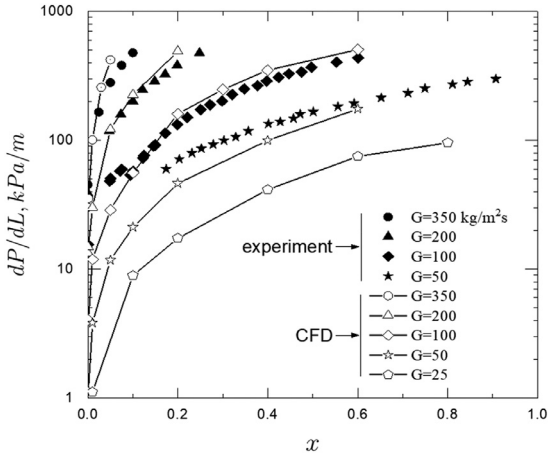

Fig. 5. Comparison of the two-phase pressure drop between the CFD prediction and the experimental measurement from (Tribbe and Müller-Steinhagen, 2001b).

(b) depicts the mean pressure along the streamwise direction. It can be noticed that the mean pressure drop stays almost linear along the flow path except for the inlet and outlet regions. Therefore the pressure drop is evaluated only within the linear range $x \in (0.2L, 0.8L)$, whereas the inlet and outlet are excluded. The strategy to determine the mean pressure drop described above will be applied for the two-phase flows as well. The Fanning friction factor is used to represent the flow friction, calculated by

$$f = \frac{\rho D_h \langle \Delta P \rangle_{linear}}{2G^2 l_{linear}} \tag{5}$$

where $\langle \Delta P \rangle$ is the time-averaged pressure drop of the linear range, and l_{linear} is the length of the linear range. Fig. 4 plots the friction factor for single-phase flow predicted using CFD, correlations and experimental results from previous works. The geometric parameters for each study are compiled in Table 2. Note that the definition of the hydraulic diameter and the friction factor sometimes differ from one literature study to another. For consistency, the original data appearing in the literature (Jin and Hrnjak, 2017; Focke et al., 1985) have been revised according to the definition in the present paper. As shown, the CFD results are close to the experimental measurements from Jin and Hrnjak (2017) and Focke et al. (1985). In addition, the CFD results conform with the (Martin, 1996) semi-theoretical correlation. The results for water and air cases reflect the fact that the friction factor is independent of the fluid properties (a charter of Newtonian fluids). A simple single-phase correlation is proposed as follows with respect to the CFD results.

$$f = 35.55 Re^{-0.972} + 0.621 \tag{6}$$

3.2. Two-phase pressure drop

The present simulations are performed under the vertically upward flow condition. Five levels of mass flux (25, 50, 100, 200, 350 kg/m^2 s) were tested, with the gas quality x varying in a broad range $0.0001 \le x \le 0.6$. The mean pressure drop per unit length is compared with the experimental results in Fig. 5; both are in reasonable agreement in most cases. However, the deviation between the experiment and the simulation becomes significant when the mass flux and gas quality get higher. This may occur because of many reasons, and the measurement error and flow maldistribution effect in the experimental tests may be one of them. From the numerical side, the pressure gradient along the channel is large at high mass flux and high gas quality, which means the compression of the gas phase would be significant, whereas this effect is not included in our simulation.

The Lockhart–Martinelli method is widely used to calculate the pressure drop in a two-phase flow system by introducing

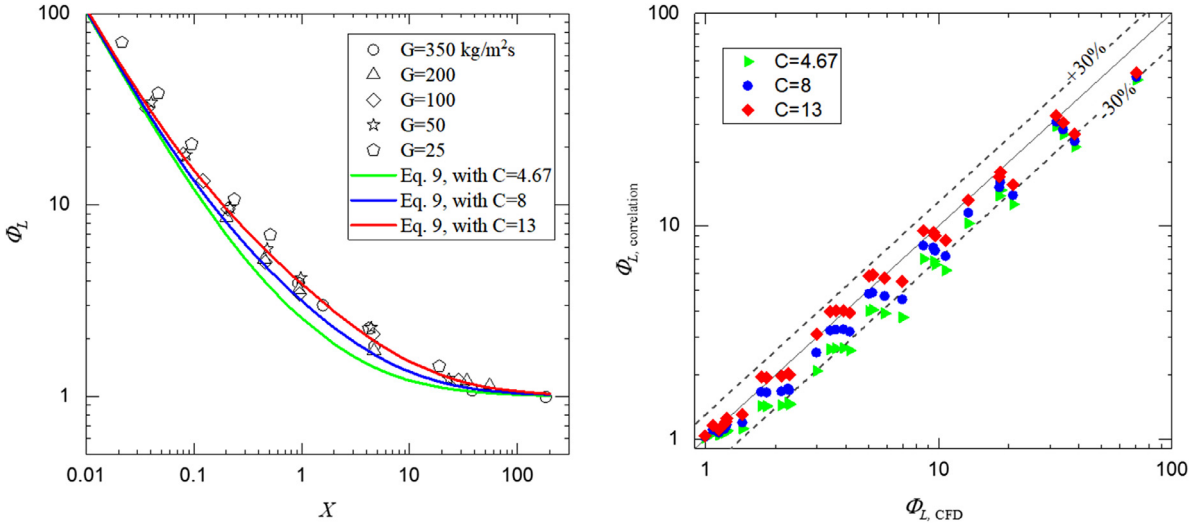

Fig. 6. The calibration of the model constant of the two-phase multiplier (left); the deviations between the correlation and the CFD data (right).

a parameter of the two-phase multiplier (Lockhart and Martinelli, 1949). The two-phase multiplier correlates the single-phase pressure drops of each phase to the two-phase pressure drop in the following way. The Lockhart–Martinelli parameter X and the multiplier ϕ_L are defined as

$$X = \sqrt{\left(\frac{dP}{dz}\right)_l \Big/ \left(\frac{dP}{dz}\right)_g} \tag{7}$$

$$\phi_L^2 = \left(\frac{dP}{dz}\right)_{lg} \Big/ \left(\frac{dP}{dz}\right)_l \tag{8}$$

respectively, where dP/dz is the pressure drop per unit length, and the subscripts "l", "g" and "lg" denote the liquid phase, gas phase, and liquid–gas two-phase, respectively.

In general, for two-phase channel flow, a unified correlation between X and ϕ_L^2 could be found, which is always shown in the form of

$$\phi_L^2 = 1 + \frac{C}{X} + \frac{1}{X^2} \tag{9}$$

where C is an empirical constant depending on the properties of the flow system. The determination of this constant bears the success of the multiplier method in predicting the two-phase pressure drop. Tribbe and Müller-Steinhagen (2001a) suggest $C = 8$ for the PHE with $\varphi = 60°$. In another relevant work, Palm and Claesson (2006) suggested $C = 4.67$ in respect to their experimental data. It should be noted that the multiplier method requires the single-phase pressure drop to be precisely calculated a priori. Tribbe and Müller-Steinhagen (2001a) did not provide the single-phase formula used for the friction factor calculation, hence their derived multiplier could not be directly used. Palm and Claesson (2006) adopted the (Martin, 1996) correlation for evaluation of the single-phase pressure drop, while they did not examine whether the correlation complies with their experimental conditions. In the present paper, the single-phase pressure is calculated by using Eq. (6), which is more compatible with the two-phase pressure drop resulting from CFD. In Fig. 6, the diagram of ϕ_L versus X is plotted by including all the CFD results. As shown, the ϕ_L and X can be well correlated by Eq. (9) if an appropriate C is used. Apparently, the values of C suggested by Palm and Claesson (2006), Tribbe and Müller-Steinhagen (2001a) are too small to correlate the CFD results correctly. We suggest a larger $C = 13$, which leads to a better multiplier to correlate with the CFD data, with the deviation less than 30%, as shown in Fig. 6.

4. Flow patterns

A range of flow patterns were captured by the CFD simulations. The massive images of flow patterns resulting from the CFD simulations are included in the supplementary material. Here we only select a few representative cases for analysis and discussion with the aim of providing a better understanding of the two-phase flows in the PHE. In this section, we make comparisons between the calculated flow patterns with the experimental evidence in open literature whenever possible. The geometry, fluid and operating conditions for the CFD simulations may differ from the counterpart experiments, so the comparison should not be considered as a strict validation, but rather a proof of concept.

4.1. Bubbly flow

Bubbly flows are recognized at very low gas quality. Fig. 7 shows representative bubbly flow patterns obtained from CFD simulations and the experimental visualizations (Grabenstein et al., 2017; Polzin et al., 2016; Solotych et al., 2016). The comparisons verify that the main characteristics of bubbly flows in the cross-corrugated channel can be captured by the CFD simulation. For a given PHE configuration, the bubble size, topology and spatial distribution are dependent on both the mass flux and gas quality. The bubble size tends to be smaller and uniform at higher mass flux because of the associated high turbulence that causes the breakup of large bubbles. Taking the case of $G = 350$ kg/m^{2}s, $x = 0.0001$ as an example, as seen, a large bubble is produced at the entrance region, which is then destroyed soon after due to the strong turbulence. For $G = 200$ kg/m^{2}s, $x = 0.0002$, an interesting phenomenon is seen; relatively large bubbles are frequently produced and reside in between the contact corners where the spacing of the plate is the maximum. Such a typical bubble behavior is also reported in the experimental works of Solotych et al. (2016). Our results indicate that a wake-like region with reduced pressure is established behind the contact corner, so that the gas bubble can be trapped in this region by the local pressure gradient. For a low total mass flux situation, the dominating bubbles are large in size, with the diameter approximate to the local spacing of the channel. The bubble is deformed dramatically as it proceeds downstream. It either breaks down, or merges with others, or becomes elongated, manifesting similar behavior as that observed by Kim et al. (2019). Nevertheless, so far, the understanding of bubble dynamics in cross-corrugated channels is fairly shallow. A detailed

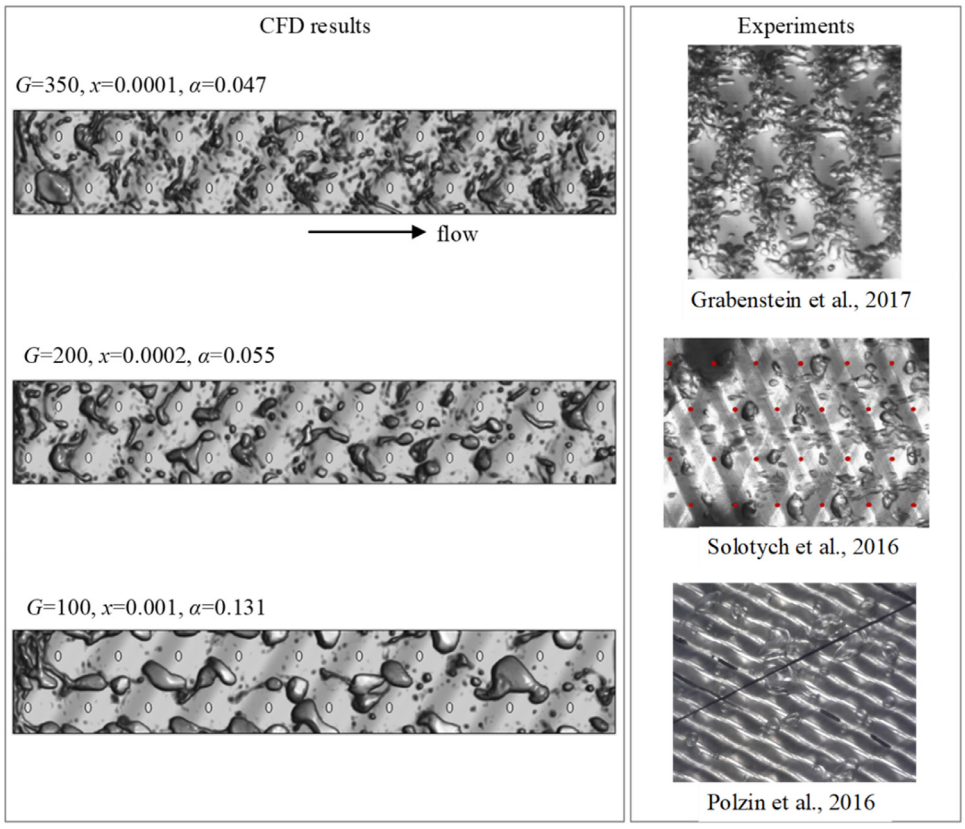

Fig. 7. Bubbly flow patterns obtained from CFD simulations and experiments.

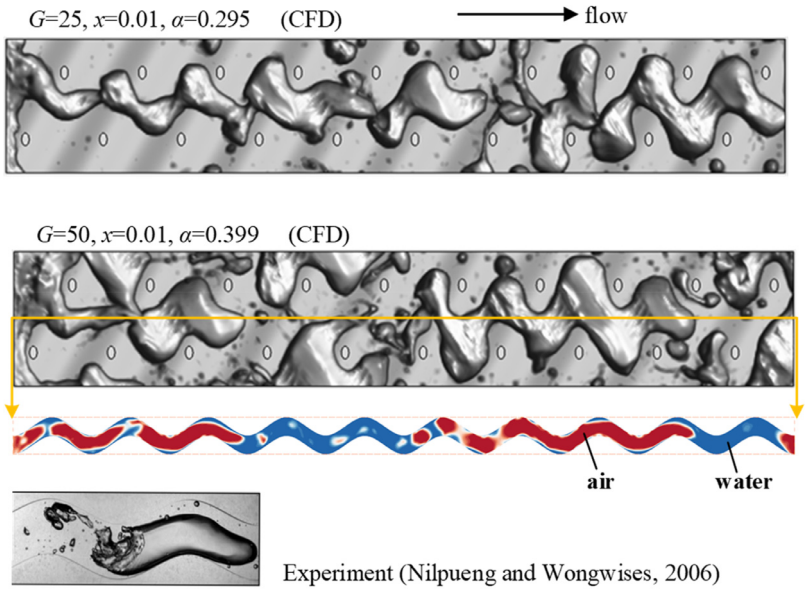

Fig. 8. Slug flow patterns predicted by CFD simulations, and a comparison to the Taylor bubble observed in a wavy channel by Nilpueng and Wongwises (2006). The blue-red contour shows the water-air distribution in a spanwise cross-section.

investigation focusing on bubble behavior is the subject of further work.

4.2. Slug flow

By increasing the gas quality, the bubbly flow transforms into a slug flow pattern, as shown in Fig. 8. The Taylor bubble in a cross-corrugated channel shows an interesting wavy appearance with a cap front. The bubble is essentially shaped by the geometry of the channel because the cross-section geometry of the channel varies vastly along the streamwise direction. Such Taylor bubbles can be as long as two times the wavelength of the corrugated plate. We did not find any publications reporting such wavy slug patterns in the PHE, which is probably due to the fact that the slug flow is not prevalent in cross-corrugated channels. It is interesting to see that, in the spanwise cross-section, the slug manifests itself resembling the Taylor bubbles observed in a parallel wavy channel by Nilpueng and Wongwises (2006), except that the slug in

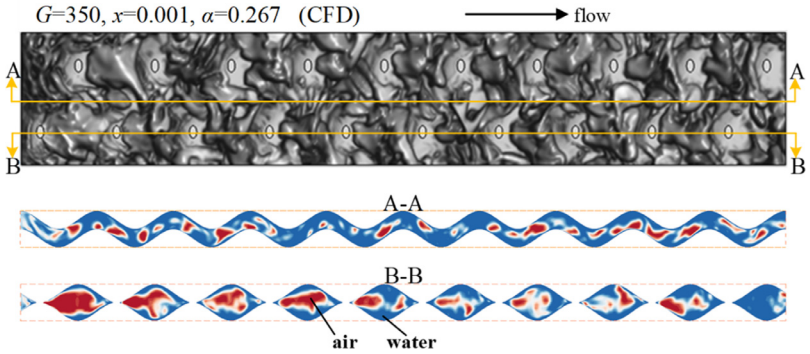

Fig. 9. Churn flow pattern predicted by CFD simulations. The chaotic feature is also described by the void fraction contours in spanwise cross-sections.

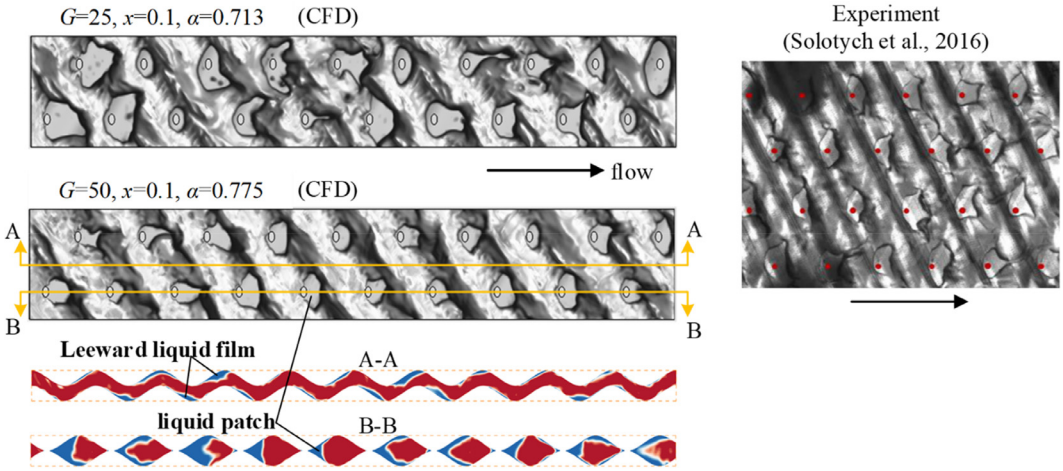

Fig. 10. Film flow with liquid patches formed behind the contact corners, and a comparison to experimental pattern in spanwise cross-sections (Solotych et al., 2016).

the cross-corrugated channel is deformed in the spanwise direction intricately due to the geometric constraint. Another unique feature of the wavy slug bubble differing from the generally observed Taylor bubble, is that the liquid film surrounding the bubble is highly non-uniform. In the deep valley of the corrugated furrows, a very thick liquid rivulet is there because of the local recirculation, whereas the liquid film is relatively thinner over the crest of the corrugation due to the strong local shear stress.

4.3. Churn flow

We did not find well-defined slug patterns at high mass flux when $G = 350$ kg/m^{2}s. Instead, a chaotic flow pattern is obtained for a gas quality as low as 0.001, as illustrated in Fig. 9. The two phases interact with each other in a very chaotic manner. The interface is highly disordered and intricate. This pattern can be treated as a vastly disrupted slug flow, and the disturbance is so intense that the slug bubbles could not survive, but break up into irregular gas clusters disorderly penetrating in the core of the channel. Such a chaotic pattern is then termed as churn flow in the present paper. It is only possible for the churn pattern to occur at very high mass flux when a high turbulence environment is established, whereas it was not found for those cases with $G \leq 200$ kg/m^{2}s.

4.4. Film flow

4.4.1. Film flow with liquid patches

The slug bubbles would be merged together as the void fraction increases over a certain threshold value, forming an interesting flow pattern shown in Fig. 10. This pattern is mainly characterized by a fan-shaped liquid patch behind each contact corner, which is evidenced by the experimental visualization of Solotych et al. (2016) and also observed by Jin (2017) during the flow evaporation in the PHE. The liquid patches decrease in size as the gas quality increases. For a given gas quality, the patch can be more stable and bigger for lower mass flux. In addition to the patch, it can also be seen that the liquid film over the wall is non-uniform. The film is much thicker over the leeside of the corrugated plate relative to the flow direction, whereas the liquid layers on the windward side of the plate (near the crest) are extremely thin. This finding is in agreement with observations by Nilpueng and Wongwises (2010).

The patches apparently exist under the low mass flux condition, whereas they are hardly seen when $G = 350$ kg/m^{2}s. The formation of the liquid patch is attributed to the wake established behind the contact corner. The liquid resides rather stably within the wake zone. The shear force from the high-speed gas core, acting on the patch interface, can hold up the liquid patch against gravity (the wall structure also plays a role in holding up the liquid patch). For very high mass flux and high gas quality, the shear force becomes so intense that it breaks down the liquid patch. That is why the liquid patch does not appear for those cases with high mass flux and relatively high gas quality.

4.4.2. Film flow with partial dry-out

By increasing the gas quality to an even high level, the liquid patches are diminished gradually, and all simulated cases go towards an almost unified film pattern, as shown in Fig. 11. For this pattern, the liquid film mainly covers the leeside of the corrugated plate. On the other hand, a large area of liquid film on the plate

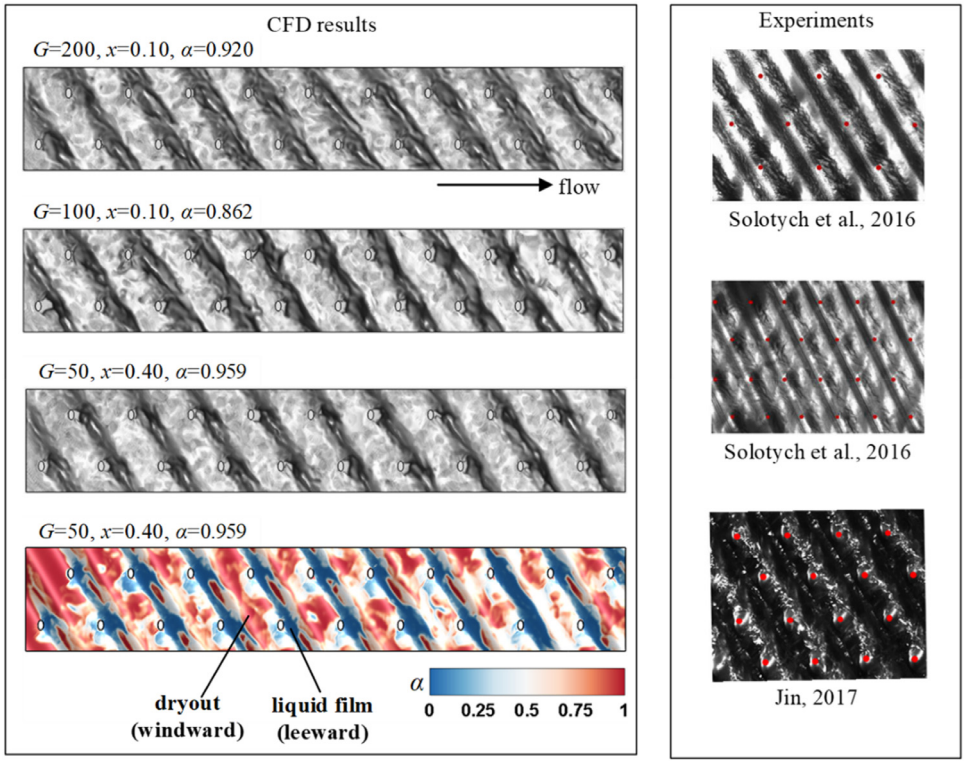

Fig. 11. Film flow with partial dry-out predicted by CFD (left). The colored contour is the void fraction in vicinity of the wall, which highlights the dry-out surface. The right side lists some experimental evidence of the film patterns.

windward is dispelled due to the strong shear stress on this side. Therefore, the plate surface is partial dry-out and directly exposed to the gas flow. This pattern should be the final stage of the flow pattern transition. In other words, all liquid–gas flows in a cross-corrugated channel will finally be settled in this film regime when the gas quality continually increases, for example, with the flow evaporation process. As long as it is formed, the further increase of gas quality only varies the film thickness, the rate of liquid entrainment and the area of the dry-out surface.

5. Flow regime map

All the simulated results are collected in a sketched flow regime map, as shown in Fig. 12 . The principle for drafting this map is based partially on the classical flow transition criteria suggested by Taitel et al. (1980). It should be noted that the boundary lines between regimes are superficially plotted in Fig. 12, because the dataset is still not sufficient enough to indicate the specific location of these boundaries. Moreover, theoretical models to predict these boundaries are still unrealizable due to the lack of fundamental understanding of the two-phase flow in the cross-corrugated geometry. Note that the transition zone in Fig. 12 denotes a combination of slug flow and film flow, because the flow is in the middle of the transition between them. Readers can find the pattern images for each regime in the supplementary material.

By comparing Fig. 12 with the flow regime map of the vertical pipe flow (Taitel et al., 1980), the two maps share some similar nature in terms of the layout of each regime. In particular, the bubble-slug boundary line is adopted directly from Taitel's map, which fits well with the cross-corrugated geometry. The transition from bubbly flow to slug flow can be interpreted as a consequence of frequent bubble aggregation due to the growing bubble density. As the slug bubble population is increased along with the gas quality, the slug bubbles merge together forming an interconnected

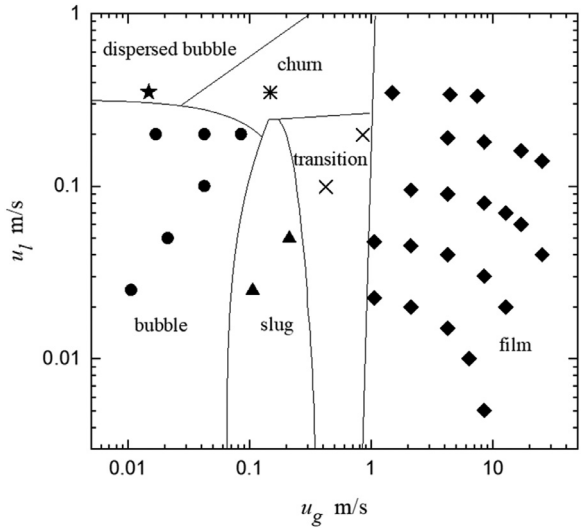

Fig. 12. A sketch of the flow regime map for water-air upward flow in the cross-corrugated channel based on CFD results. The detailed flow patterns corresponding to each scatter in the map can be found in the supplementary material.

gas core, confined by the wall liquid film. So the film regime in the cross-corrugated channel corresponds to the annular regime for tube flow. Even though the dispersed bubbly flow is only observed for the case with $G = 350$ kg/m^{2}s, $x = 0.0001$, we conjecture that above the boundary line between the bubble regime and the dispersed bubble regime, it is only possible for dispersed small bubbles to be generated in the cross-corrugated channel. This is because the turbulence promoted by the cross-corrugated geometry is so strong that it breaks the bubbles into very small sized ones sustainably, also explaining why the critical liquid superficial

velocity u_l corresponding to this transition is almost an order of magnitude lower than that of the pipe flow. At high mass flux, the high turbulent environment prohibits the formation of smooth shaped slug bubbles. Instead, the dispersed bubbles aggregate into chaotic patterns when the gas flux is increased, driving the flow into the churn regime. The entire right side of the map should be the film regime, and the transition to this regime is fairly quick and only requires very low gas quality. As shown in Fig. 12, the critical superficial gas velocity for the transition to film pattern is around $u_g = 1.0$m/s, whereas it is 15m/s for upward liquid–gas flow in a pipe (Taitel et al., 1980).

6. Mean void fraction

The void fraction is a crucial variable to characterize the two-phase flows. However, it is tricky to measure it directly by the experiment. A so-called homogeneous void fraction model is given as

$$\frac{1}{\alpha} = 1 + \frac{1-x}{x}\left(\frac{\rho_g}{\rho_l}\right)^n \tag{10}$$

which is one of the most widely applied models for the prediction of void fraction in two-phase flow systems. It was also adopted to evaluate the void fraction in PHEs (Grabenstein et al., 2017; Jin, 2017). However, the CFD results suggest that this model causes unacceptable error in predicting the void fraction in the PHE; see Fig. 13. Therefore, an appropriate void fraction predicting model is needed for the PHE. In this paper, a suitable void fraction model for the PHE is recognized based on the results of the CFD simulations. For the CFD simulation, the mean void fraction can be calculated by

$$\alpha = \frac{1}{V}\int \alpha_g dV = \frac{1}{V}\sum_{i=1}^{n} (\alpha_g)_i V_i \tag{11}$$

where V represents the volume of the entire domain, and V_i denotes the volume of the ith computational cell. Fig. 13 presents the calculated void fraction α. It can be seen that α shows a strong dependence on both x and G. Apparently, Eq. (10) fails to account for the role of G. Then the void fraction model of Zuber and Findlay (2012) was tested. This model has been developed to estimate the mean void fraction of a two-phase flow system by accounting for the effects of both the heterogeneous distribution profile and the drift velocity between the phases. The model is given as

$$\alpha = \frac{u_g}{C_0 u_m + u_{dr}} \tag{12}$$

where u_g is the gas superficial velocity, and u_m is the mean superficial velocity, $u_m = G\rho_m$. Specifically, C_0 is the distribution parameter, which needs to be calibrated according to the properties of the two-phase flow system. It is suggested that for the pipe flow, C_0 varies in the range of $0.95 < C_0 \leq 1.2$, depending on the profile of the radial distribution of the void fraction (Guet and Ooms, 2005). The u_{dr} denotes the drift velocity between two phases, given in the form

$$u_{dr} = 1.53\left(\frac{g\sigma\Delta\rho}{\rho_l^2}\right)^{1/4} \tag{13}$$

Fig. 13 indicates that the Eq. (12) is able to correlate reasonably well the void fraction to the vapor quality by setting $C_0 = 1.2$. The relative deviation is below 20% for the case with $\alpha \geq 0.25$, while large deviation appears if $\alpha < 0.25$. Note that $\alpha = 0.25$ is often noted as a critical value for the transition from bubbly flow to slug flow in pipes (Taitel et al., 1980). Furthermore, the results suggest that when the flow enters the film regime, α becomes greater than approximately 0.68, and Eq. (12)tends to under-predict the α, which indicates the performance of the model depends somehow on the fluid regimes. In this respect, the model constant needs to be tuned in order to evaluate better the void fraction in the PHE. The modified version is given as

$$\alpha = \frac{u_g}{C_0 u_m + C_1 u_{dr}} \tag{14}$$

with

$$C_0 = 1.03\left(\frac{1-x}{x}\right)^{0.02},\ C_1 = 1 \quad \text{for}\ \alpha \geq 0.25$$

and

$$C_0 = 1.03\left(\frac{1-x}{x}\right)^{0.02},\ C_1 = \left(\frac{1-x}{x}\right)^{0.125} \quad \text{for}\ \alpha < 0.25$$

As shown in Fig. 13(b), the modified model yields a better prediction of the mean void fraction in this cross-corrugated channel with the deviation far less than 20% for the most cases.

In Fig. 13, the flow regimes are classified on the plot by the dash boundary lines. It seems that the void fraction can be used as a discriminant to distinguish the flow regimes in cross-corrugated channels. For instance, it is bubbly flow if $\alpha < 0.25$, and it is most likely to be film flow if $\alpha > 0.68$. Hence, it would be possible to derive a void fraction based discriminant for flow regimes. That would make the ascertaining of flow regimes in the PHE more straightforward and easier.

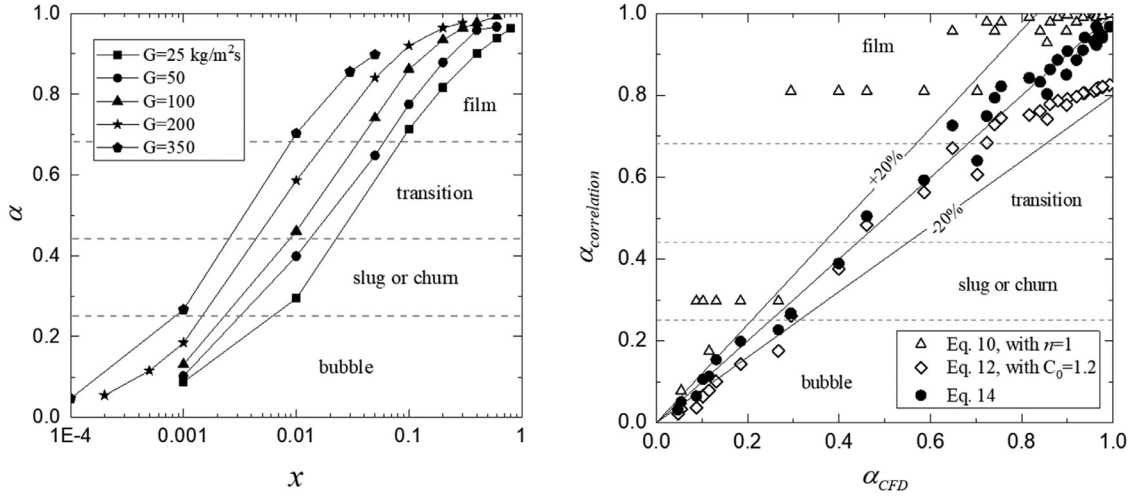

Fig. 13. Computed mean void fraction α versus the gas quality x at different mass fluxes G (left side); the deviation of different void fraction models from the CFD results (right side).

7. Conclusions

A pioneering CFD study of upward two-phase flow in a vertical cross-corrugated channel was presented in this paper. The study aims to enable a better understanding of the liquid–gas flow in corrugated plate heat exchangers. The simulations cover a broad range of operating conditions with $25 \leq G \leq 350\,\mathrm{kg/m^2s}$ and $0.0001 \leq x \leq 0.8$. A variety of flow patterns in the channel were successfully modeled and analyzed. The hydraulic aspects of the adiabatic two-phase flow in the cross-corrugated channel were also investigated.

The two-phase flow friction in the cross-corrugated channel was calculated from the CFD simulation. The friction factor can be well correlated by the Lockhart–Martinelli method. The two-phase multiplier was calibrated based on the CFD data. The CFD simulation also yields a reliable dataset of the mean void fraction in the cross-corrugated channel. The Zuber and Findlay model is able to correlate the mean void fraction well with the gas quality and the mass flux. The model was further modified to reduce the deviation from the CFD data. The two-phase multiplier (Eq. (6)–(9)) and the modified Zuber and Findlay model (Eq. (14)) are recommended for estimating the pressure drop and the mean void fraction in plate heat exchangers ($\varphi \approx 60^\circ$), respectively.

A flow regime map was drafted based on CFD resolved flow patterns. The map is divided into six regimes including bubble, dispersed bubble, slug, churn, transition and film flows. Most of these flow patterns are verified by experimental evidence from literature reviews. Bubbly flows occur in the cross-corrugated channel when void fraction $\alpha < 0.25$. With the increase of void fraction, the bubbly flow switches into either a slug flow or a churn flow pattern, depending on the total mass flux. When $\alpha > 0.68$, the two-phase flows are unexceptionally settled in the film flow regime regardless of the total mass flux.

In summary, this study has proved the capability and advantages of using CFD to study complex two-phase flows in the cross-corrugated channel. The numerical results complement state-of-the-art in two respects: numerical quantification of the mean void fraction and the friction factor; and numerical exposition of diverse liquid–gas flow patterns in the cross-corrugated channel.

Declaration of Competing Interest

The authors declared that there is no conflict of interest.

Acknowledgement

This project has received funding from the European Union's Horizon 2020 research and innovation programme under the Marie Skłodowska-Curie grant agreement number 713683. The financial support is gratefully acknowledged.

References

Amalfi, R.L., Vakili-Farahani, F., Thome, J.R., 2016. Flow boiling and frictional pressure gradients in plate heat exchangers. Part 1: review and experimental database. Int. J. Refrig. 61, 166–184. doi:10.1016/j.ijrefrig.2015.07.010.

ANSYS, I., 2018. ANSYS Fluent Theory Guide v18.2. ANSYS 18.2 Doc.

Brackbill, J.U., Kothe, D.B., Zemach, C., 1992. A continuum method for modeling surface tension. J. Comput. Phys. 100, 335–354.

Egorov, Y., 2004. Contact condensation in stratified steam-water flow. Valid. CFD codes with PTS-relevant test cases-EVOL-ECORA D 7.

Focke, W.W., Zachariades, J., Olivier, I., 1985. The effect of the corrugation inclination angle on the thermohydraulic performance of plate heat exchangers. Int. J. Heat Mass Transf. 28, 1469–1479. doi:10.1016/0017-9310(85)90249-2.

Grabenstein, V., Polzin, A.E., Kabelac, S., 2017. Experimental investigation of the flow pattern, pressure drop and void fraction of two-phase flow in the corrugated gap of a plate heat exchanger. Int. J. Multiph. Flow 91, 155–169. doi:10.1016/j.ijmultiphaseflow.2017.01.012.

Gradeck, M., Lebouché, M., 2000. Two-phase gas–liquid flow in horizontal corrugated channels. Int. J. Multiph. Flow 26, 435–443. doi:10.1016/S0301-9322(99)00018-X.

Guet, S., Ooms, G., 2005. Fluid mechanical aspects of the gas-lift technique. Annu. Rev. Fluid Mech. 38, 225–249. doi:10.1146/annurev.fluid.38.061505.093942.

Hsieh, Y.Y., Chiang, L.J., Lin, T.F., 2002. Subcooled flow boiling heat transfer of R-134a and the associated bubble characteristics in a vertical plate heat exchanger. Int. J. Heat Mass Transf. 45, 1791–1806. doi:10.1016/S0017-9310(01)00294-0.

Jin, S., 2017. A New Experimental Approach of Characterizing Two Phase Flow and Heat Transfer in Plate Heat Exchangers. University of Illinois, Urbana-Champaign at.

Jin, S., Hrnjak, P., 2017. A new method to simultaneously measure local heat transfer and visualize flow boiling in plate heat exchanger. Int. J. Heat Mass Transf. 113, 635–646. doi:10.1016/j.ijheatmasstransfer.2017.04.116.

Kharangate, C.R., Lee, H., Mudawar, I., 2015. Computational modeling of turbulent evaporating falling films. Int. J. Heat Mass Transf. 81, 52–62.

Kharangate, C.R., Mudawar, I., 2017. International journal of heat and mass transfer review of computational studies on boiling and condensation. Int. J. Heat Mass Transf. 108, 1164–1196. doi:10.1016/j.ijheatmasstransfer.2016.12.065.

Kim, H.J., Liebenberg, L., Jacobi, A.M., 2019. Flow visualization of two-phase R-245fa at low mass flux in a plate heat exchanger near the micro-macroscale transition. Sci. Technol. Built Environ. 1–12.

Lee, D., Kim, D., Yun, S., Kim, Y., 2019. Two-phase flow patterns and pressure drop of a low GWP refrigerant R-1234ze (E) in a plate heat exchanger under adiabatic conditions. Int. J. Heat Mass Transf. 145, 118816.

Lockhart, R.W., Martinelli, R.C., 1949. Proposed correlation of data for isothermal two-phase, two-component flow in pipes. Chem. Eng. Prog. 45, 39–48.

Martin, H., 1996. A theoretical approach to predict the performance of chevron-type plate heat exchangers. Chem. Eng. Process. Process Intensif. 35, 301–310. doi:10.1016/0255-2701(95)04129-X.

Menter, F.R., 1994. Two-equation eddy-viscosity turbulence models for engineering applications. AIAA J. 32, 1598–1605.

Nilpueng, K., Wongwises, S., 2010. Two-phase gas–liquid flow characteristics inside a plate heat exchanger. Exp. Therm. Fluid Sci. 34, 1217–1229. doi:10.1016/j.expthermflusci.2010.05.001.

Nilpueng, K., Wongwises, S., 2006. Flow pattern and pressure drop of vertical upward gas–liquid flow in sinusoidal wavy channels. Exp. Therm. Fluid Sci. 30, 523–534. doi:10.1016/j.expthermflusci.2005.10.004.

Palm, B., Claesson, J., 2006. Plate heat exchangers: calculation methods for singleand two-phase flow. Heat Transf. Eng. 27, 88–98.

Polzin, A.E., Kabelac, S., De Vries, B., 2016. Two-phase flow patterns in adiabatic and diabatic corrugated plate gaps. Journal of Physics: Conference Series. IOP Publishing 32111 doi:10.1088/1742-6596/745/3/032111.

Sacher, J., Repke, J.-.U., 2019. Development of a mesoscale model for the gas phase fluid dynamics in structured packings based on fundamental experiments and CFD investigations. Chem. Eng. Res. Des. doi:10.1016/j.cherd.2019.04.032.

Singh, R.K., Galvin, J.E., Sun, X., 2018. Multiphase flow studies for microscale hydrodynamics in the structured packed column. Chem. Eng. J. 353, 949–963. doi:10.1016/j.cej.2018.07.067.

Solotych, V., Lee, D., Kim, J., Amalfi, R.L., Thome, J.R., 2016. Boiling heat transfer and two-phase pressure drops within compact plate heat exchangers: experiments and flow visualizations. Int. J. Heat Mass Transf. 94, 239–253. doi:10.1016/j.ijheatmasstransfer.2015.11.037.

Sun, B., He, L., Liu, B.T., Gu, F., Liu, C.J., 2013. A new multi-scale model based on CFD and macroscopic calculation for corrugated structured packing column. AIChE J. 59, 3119–3130. doi:10.1002/aic.14082.

Taitel, Y., Bornea, D., Dukler, A.E., 1980. Modelling flow pattern transitions for steady upward gas–liquid flow in vertical tubes. AIChE J. 26, 345–354.

Tao, X., Nuijten, M.P., Infante Ferreira, C.A., 2017. Two-phase vertical downward flow in plate heat exchangers: flow patterns and condensation mechanisms. Int. J. Refrig. 85, 489–510. doi:10.1016/j.ijrefrig.2017.10.008.

Tribbe, C., Müller-Steinhagen, H.M., 2001a. Gas/Liquid flow in plate-and-frame heat exchangers – part II: two-Phase multiplier and flow pattern analysis. Heat Transf. Eng. 22, 12–21. doi:10.1080/01457630150215686.

Tribbe, C., Müller-Steinhagen, H.M., 2001b. Gas/Liquid flow in plate-and-frame heat exchangers – part I: pressure drop measurements. Heat Transf. Eng. 22, 5–11. doi:10.1080/01457630150215677.

Vlasogiannis, P., Karagiannis, G., Argyropoulos, P., Bontozoglou, V., 2002. Air-water two-phase flow and heat transfer in a plate heat exchanger. Int. J. Multiph. Flow 28, 757–772. doi:10.1016/S0301-9322(02)00010-1.

Xu, X., Carey, V.P., 1987. Heat transfer and two-phase flow during convective boiling in a partially-heated cross-ribbed channel. Int. J. Heat Mass Transf. 30, 2385–2397. doi:10.1016/0017-9310(87)90229-8.

Zuber, N., Findlay, J.A., 2012. Average volumetric concentration in two-phase flow systems. J. Heat Transf. 87, 453. doi:10.1115/1.3689137.